Vibrational CARS measurements in a near-atmospheric pressure plasma jet in nitrogen: I. Measurement procedure and results

OPEN ACCESS
IOP Publishing
Journal of Physics D: Applied Physics
J. Phys. D: Appl. Phys. **54** (2021) 305204 (16pp)
https://doi.org/10.1088/1361-6463/abfd6b

Vibrational CARS measurements in a near-atmospheric pressure plasma jet in nitrogen: I. Measurement procedure and results

J Kuhfeld*, N D Lepikhin, D Luggenhölscher and U Czarnetzki*

Ruhr University Bochum, Institute for Plasma and Atomic Physics, Bochum, Germany

E-mail: jan.kuhfeld@rub.de and uwe.czarnetzki@rub.de

Received 26 January 2021, revised 7 April 2021
Accepted for publication 30 April 2021
Published 25 May 2021

Abstract

The non-equilibrium ro-vibrational distribution functions of molecules in a plasma can heavily influence the discharge operation and the plasma-chemistry. A convenient method for measuring the distribution function is coherent anti-Stokes Raman scattering (CARS). CARS spectra are measured in a ns-pulsed plasma between two parallel, 1 mm spaced molybdenum electrodes in nitrogen at 200 mbar with pulse durations of 200 ns/250 ns and a repetition rate of 1 kHz. The CARS spectra are analyzed by a fitting routine to extract information about the vibrational excitation of the nitrogen molecules in the plasma. It is found that during the discharge the vibrational distribution for $v \lesssim 7$ can be described by a vibrational two-temperature distribution function. Additionally, the electric field is measured by the electric field induced second harmonic generation method during the discharge pulse. It is found to be constant in time after the initial ionization wave with values close to 81 Td for the investigated conditions. During the afterglow between two discharge pulses a more general fitting approach is used to obtain the population differences of two neighboring vibrational states. This allows to capture the more complex vibrational dynamics in that time period. The measurement results are discussed in more detail and compared to simple plasma models in a companion paper Kuhfeld *et al* (2021 *J. Phys. D: Appl. Phys.* **54** 305205).

Keywords: coherent anti-Stokes Raman scattering, CARS spectroscopy, ro-vibrational non-equilibrium, ro-vibrational distribution function, APPJ, nitrogen plasma

(Some figures may appear in colour only in the online journal)

* Authors to whom any correspondence should be addressed.

1. Introduction

For several years atmospheric pressure plasmas are a very active research topic with respect to multiple practical applications, e.g. plasma assisted ignition [1, 2], plasma catalysis [3–6] and plasma medicine [7–10]. Many of these applications depend on the unique chemical properties of atmospheric pressure plasmas, which have their roots in the different non-equilibrium conditions in these kinds of discharges [11]. A very important non-equilibrium can be found in the vibrational distribution functions (VDFs) of molecular plasmas. Strong excitation through resonant interaction with the plasma electrons and the anharmonicity of the vibrational potential usually lead to a strong overpopulation of the higher vibrationally excited states compared to a Boltzmann distribution [11]. On the other hand the translational and rotational temperatures can be very low (close to room temperature) due to the low coupling of the electrons to the translational and rotational degrees of freedom of the molecules and slow vibrational–translational (V–T) relaxation [11]. This means that energy to be used in chemical reactions can be stored in the gas without increasing the translational temperature. There are several ways how this can be leveraged in industrial applications. For example catalysts could potentially be used at gas temperatures below their traditional operating temperature, which could increase their durability and efficiency [6, 12]. Another process of interest over the last years is carbon dioxide dissociation by step wise vibrational excitation, which might be more efficient than direct dissociation by electron impact [13–15].

All these examples clearly state an interest in tailoring the vibrational excitation in a plasma for the specific application by using different plasma sources, e.g. (surface) dielectric barrier discharges, plasma jets or micro-structured array devices. For this purpose the influence of the plasma parameters on the VDF needs to be understood in detail, so kinetic modeling as well as detailed measurements need to be performed in parallel for different discharge types and conditions.

Measurements of the VDF can be performed for some gases or vibrational modes by TDLAS or FTIR [6, 12, 16], but this is not possible in other cases as e.g. nitrogen or the symmetric stretch mode of carbon dioxide. In these cases other methods need to be employed like spontaneous Raman scattering or coherent anti-Stokes Raman scattering (CARS). A detailed description of previously performed CARS and spontaneous Raman scattering measurements in plasmas is given in [17] so here only a short summary is provided. Some of the first CARS measurements in nitrogen plasmas known to the authors were performed in low pressure DC discharges for example by Shaub *et al* [18] who also developed a scheme for the evaluation of CARS spectra with non-Boltzmann vibrational distributions. Their scheme is valid under the assumption that the bulk of the molecules follows a Boltzmann distribution and only a very small number is excited to higher vibrational states, leaving the distribution of the bulk. This might be the case for low pressure DC discharges but for pulsed high current plasmas a significant amount, i.e. in the range of some 10%, of the molecules can be excited during one pulse.

Measurements in pulsed nitrogen plasmas were performed among others by Valyansky *et al* [19], Deviatov *et al* [20], Vereshchagin *et al* [21], and Montello *et al* [22]. In general the vibrational excitation in these works can be described on three timescales: The excitation during the discharge (mainly) by resonant electron collisions usually happens on timescales of nanoseconds, the redistribution of vibrational–vibrational (V–V) transfer collisions in the first microseconds after the pulse and the loss of vibrational excitation by diffusion or deactivation at the walls, typically some hundreds of microseconds or a few milliseconds after the discharge. Depending on the experimental conditions, loss through V–T collisions can also be an important mechanism. In some of the mentioned works an increase of the lower lying vibrational excited states in the first microseconds of the afterglow was observed which could not be explained purely by V–V transfer mechanisms, leading the authors to the conclusion that quenching from metastable electronic states [20, 22] might have a significant impact on the vibrational excitation. This was not observed in [19] and [21], where no significant deviation from the populations predicted by V–V models was seen. More recently Yang *et al* [23] tried to explain the measurement results by numerical modeling but were also not able to reproduce the increase of the total number of vibrational quanta observed in the measurements. Consequently, the mechanism behind this process is still an open research question and will certainly vary for different discharge conditions and geometries.

In addition to the previous works, more recently the vibrational distribution of nitrogen was measured in microwave plasmas [24, 25] by spontaneous Raman scattering, where the effect of the gas temperature on the vibrational excitation was studied. Those works have shown, that controlling the gas temperature through pulsing the discharge can improve the efficiency of the vibrational excitation.

In this work measurements of the VDF of nitrogen are performed in a near atmospheric pressure ns-pulsed plasma jet with plane parallel molybdenum electrodes similar to the ones used in [26]. In contrast to some earlier works mentioned above the vibrational distribution is not determined by comparing the intensity of the different peaks in the CARS spectrum. Instead, it is determined by fitting a calculated spectrum, like it is traditionally done for rotational temperature measurements by CARS [27], but on a larger spectral range to capture multiple vibrational transitions. Furthermore, dual pump CARS is used instead of the more traditional approach with two degenerate pump beams, to allow simultaneous measurements in nitrogen and CO_2 in future works.

2. CARS method

2.1. CARS spectra and fitting routine

There are multiple reviews about CARS as a diagnostic method for temperature and concentration measurements in gases and other media [28–32], so here we will only give a short summary of the aspects relevant for this work. CARS is a non-linear optical process of third order, in which three electromagnetic waves with angular frequencies ω_{Pu}, ω_S and

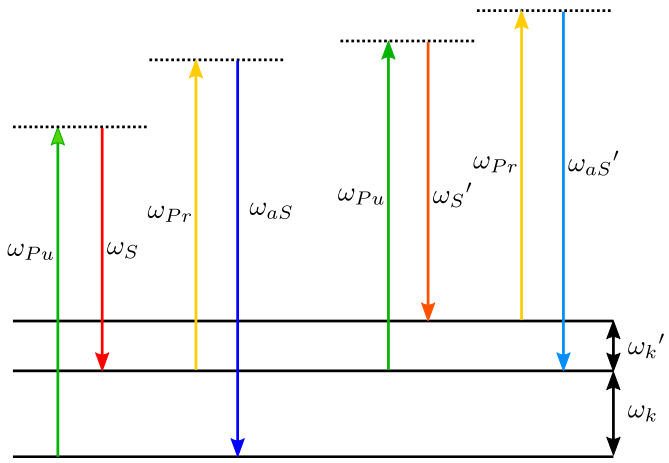

Figure 1. Energy scheme of the CARS process. ω_{pu}, ω_S, ω_{pr} and ω_{aS} denote the angular frequencies of the pump, Stokes, probe and anti-Stokes beams respectively. ω_k is the angular frequency corresponding to a vibrational transition of the probed molecule. The prime denotes a second transition with lower energy (e.g. because of the anharmonicity of the vibrational potential) requiring a slightly different Stokes $\omega_S{}'$ and anti-Stokes $\omega_{aS}{}'$ frequency.

ω_{Pr} induce a non-linear polarization in a medium at frequency $\omega_{aS} = \omega_{Pu} + \omega_{Pr} - \omega_S$. ω_{Pu}, ω_S, ω_{Pr} and ω_{aS} are called pump, Stokes, probe and anti-Stokes beam respectively. The energy scheme of the process is illustrated in figure 1 for two transitions. The process is resonant if $\omega_{Pu} - \omega_S$ is close to a state transition of the probed medium. In this work the transition energy $\hbar\omega_k$ belongs to vibrational transitions of nitrogen. The intensity of the generated anti-Stokes beam is proportional to the square of the so called CARS susceptibility and the product of the three input laser intensities:

$$I_{aS}(\omega_R) \propto |\chi_{CARS}(\omega_R)|^2 I_{Pu} I_{Pr} I_S(\omega_R) \tag{1}$$

where $\omega_R = \omega_{Pu} - \omega_S$ is the Raman shift. The CARS susceptibility in the pressure broadening regime for parallel polarized light far from electronic resonances can be written as

$$\chi_{CARS}(\omega) = \chi_{NR} + \chi_R(\omega) = \chi_{NR} + \sum_k \frac{a_k}{\omega_k - \omega - i\Gamma_k} \tag{2}$$

where the sum includes all possible ro-vibrational transitions k with the energy difference $\hbar\omega_k = E(v_{k,f}, J_{k,f}) - E(v_{k,i}, J_{k,i})$ and the linewidth (HWHM) Γ_k. The ro-vibrational energies are calculated with the Dunham coefficients given in table 1 by

$$E(v,J) = \sum_{i,j} Y_{ij} \left(v + \frac{1}{2}\right)^i (J(J+1))^j. \tag{3}$$

With the assumptions above the amplitude of the lines depend on the population difference between the lower and the upper state of the transition $\Delta N_k = N_{k,l} - N_{k,u}$ and the differential cross section for spontaneous Raman scattering:

$$a_k = \left(\frac{c^4}{\hbar\omega_S^4}\right) \Delta N_k \left.\frac{\mathrm{d}\sigma}{\mathrm{d}\Omega}\right|_k. \tag{4}$$

The Raman cross section for the Q branch ($\Delta v = 1, \Delta J = 0$) can be written as [27, 36]

$$\left.\frac{\mathrm{d}\sigma}{\mathrm{d}\Omega}\right|_Q = \left(\frac{\omega_S}{c}\right)^4 \frac{\hbar}{2\omega_0} \left[\frac{\alpha'^2}{M} + \frac{4}{45}\frac{\gamma'^2}{M} b_J^J\right] (v+1). \tag{5}$$

The cross sections for the O and S branch are given by [27, 36]

$$\left.\frac{\mathrm{d}\sigma}{\mathrm{d}\Omega}\right|_O = \left(\frac{\omega_S}{c}\right)^4 \frac{\hbar}{2\omega_0} \frac{4}{45} \frac{\gamma'^2}{M} b_{J+2}^J (v+1) C_O(J) \tag{6}$$

$$\left.\frac{\mathrm{d}\sigma}{\mathrm{d}\Omega}\right|_S = \left(\frac{\omega_S}{c}\right)^4 \frac{\hbar}{2\omega_0} \frac{4}{45} \frac{\gamma'^2}{M} b_{J-2}^J (v+1) C_S(J) \tag{7}$$

with the centrifugal force corrections [27]

$$C_O(J) = \left(1 + 4\frac{B_e}{\omega_e}\mu(2J-1)\right)^2 \tag{8}$$

$$C_S(J) = \left(1 - 4\frac{B_e}{\omega_e}\mu(2J+3)\right)^2. \tag{9}$$

In the equations above ω_0 is the oscillator frequency of the molecule, $\frac{\alpha'^2}{M}$ and $\frac{\gamma'^2}{M}$ are the squared isotropic and anisotropic derived polarizabilities over the reduced mass of the vibration, B_e and ω_e the Herzberg molecular parameters and

$$b_J^J = \frac{J(J+1)}{(2J-1)(2J+3)} \tag{10}$$

$$b_{J+2}^J = \frac{3(J+1)(J+2)}{2(2J+1)(2J+3)} \tag{11}$$

$$b_{J-2}^J = \frac{3J(J-1)}{2(2J+1)(2J-1)} \tag{12}$$

are the Placzek–Teller coefficients for diatomic molecules [36].

The constants $\frac{\alpha'^2}{M}$ and $\frac{\gamma'^2}{M}$ in (5)–(7) are calculated following the approach of [27] from experimental measurements of the Q branch cross section for $v = 0 \to 1$

$$\left.\frac{\mathrm{d}\sigma}{\Omega}\right|_{Q,v=0} \approx \frac{\hbar\omega_S^4}{2\omega_0 c^4} \frac{\alpha'^2}{M} \tag{13}$$

and the Q branch depolarization ratio

$$\rho_J = \frac{3b_{JJ}(\gamma'/\alpha')^2}{45 + 4b_{JJ}(\gamma'/\alpha')^2}. \tag{14}$$

While the line positions ω_k in (2) depend only on the molecular parameters, the linewidths Γ_k depend on the gas mixture, the pressure and the temperature. There exist multiple scaling laws for the linewidths in nitrogen, for example the so-called polynomial-differential exponential gap law or the modified

Table 1. Dunham coefficients Y_{ij} in units of cm^{-1}. The data marked with [a] is from [33], [b] from [34] and [c] from [35, 36].

$i\backslash j$	0	1	2	3
0	0	1.998[c]	-5.76×10^{-6}[c]	0
1	2358.535[a]	−0.017249[a]	-8.32×10^{-9}[b]	-2.58×10^{-13}[b]
2	−14.3074[a]	-3.24×10^{-5}[a]	-4.2×10^{-10}[b]	0
3	-4.98×10^{-3}[a]	0	0	0
4	-1.22×10^{-4}[a]	0	0	0

exponential gap law (MEGL) [37]. In general the linewidths are calculated with [37]

$$\Gamma_j = \sum_{i\neq j} \gamma_{ij}, \tag{15}$$

where γ_{ij} is the collisional transfer rate for rotational states $j \to i$. Note the different index notation compared to the one used in (2), where the index k corresponds to a transition between to ro-vibrational states. In (15) i, j correspond to rotational quantum numbers. The relation between the two notations is that—for a Q branch transition—j is the rotational quantum number which stays constant during the transition k. For O and S branch transitions the rotational quantum numbers u and l for the upper and lower state respectively are different and the linewidth for transition k is calculated as

$$\Gamma_k = \frac{1}{2}\left(\Gamma_u + \Gamma_l\right). \tag{16}$$

If the rotational states are Boltzmann distributed, detailed balance requires for the forward and reverse rates:

$$g(i)\exp(-E_i/k_BT)\gamma_{ji} = g(j)\exp(-E_j/k_BT)\gamma_{ij} \tag{17}$$

where g are the statistical weights for the rotational states. In this work the MEGL is used which gives for the uprates [37]

$$\gamma_{ji} = p\alpha\frac{1-e^{-m}}{1-e^{-mT/T_0}}\left(\frac{T_0}{T}\right)^{1/2}\left(\frac{1+1.5E_i/k_BT\delta}{1+1.5E_i/k_BT}\right)^2 \times \exp(-\beta|\Delta E_{ji}|/k_BT) \tag{18}$$

where p is the pressure in bar, $\Delta E_{ji} = E_j - E_i$ the energy difference between states j and i and T the gas temperature in K (in the following discussions assumed to be equal to the rotational temperature). The parameters for nitrogen are $\alpha = 0.0231$ cm^{-1} bar^{-1}, $\beta = 1.67$, $\delta = 1.21$, $m = 0.1487$ and $T_0 = 295$ K [37].

In this context it should be mentioned, that the line profile in (2) is only valid in low or medium pressures, as it assumes that the lines are isolated. For pressures close to atmospheric pressure this is not necessarily true and more complex line shapes are required like they are given in the rotational diffusion model or the exponential gap model [37]. To verify if the isolated line model is still appropriate under the conditions in this work (nitrogen at 200 mbar), nitrogen CARS spectra of the Q branch transition $v = 0 \to 1$ are calculated for 200 mbar and 1 bar with the CARSFT [38] software for both the isolated lines and the more complex exponential gap model. The results are compared in figure 2. While there is a noticeable difference between the isolated lines and the exponential gap model for 1 bar at low rotational quantum numbers, the curves at 200 mbar are indistinguishable. As conclusion the isolated lines model is sufficient for the conditions investigated here.

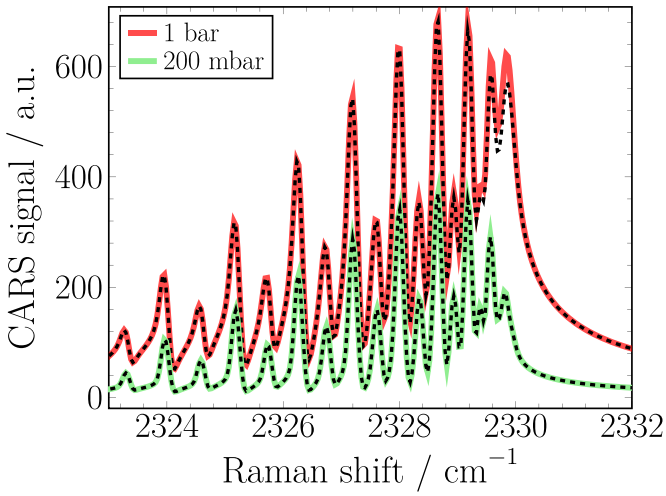

Figure 2. Comparison of spectra calculated with the isolated lines model (dashed) compared to calculations with the exponential gap model (solid) in pure nitrogen ($T = 350$ K) at 1 bar (red) and 200 mbar (blue).

As seen in (2) and (4) the intensity of the generated anti-Stokes beam depends on the population density differences of the participating states. This means by scanning the Stokes beam over multiple transitions and measuring the anti-Stokes intensity, information about the ro-VDFs can be extracted. Equivalently, a Stokes beam with a continuous broadband spectrum can be used to record the whole anti-Stokes spectrum with a single laser shot as is done in this work. One way of gaining information about the VDF is by fitting theoretically calculated spectra to the measured ones. This approach is often used in rotational temperature measurements, where the rotational structure needs to be resolved and lines can be overlapping at certain pressures or even motional narrowing [39] can occur.

For most plasma sources the vibrational and rotational temperature are typically not the same. In these cases spectrometers with a larger spectral range are used to monitor multiple vibrational lines. This usually results in a lower spectral resolution so that the rotational structure of the lines can not be resolved.

A popular approach to determine the vibrational distribution from these low-resolution spectra is to first normalize the spectrum to either the Stokes laser spectrum or a non-resonant spectrum from another gas without vibrational resonances in that wavelength region. Then the square root of the normalized spectrum is taken and for each transition the integral over the corresponding peak $I_{v,v+1}$ is calculated. Under the assumption that the non-resonant and the real part of the resonant susceptibility are negligible compared to the imaginary part of the resonant susceptibility, it follows that

$$I_{v,v+1} \propto \Delta N_{v,v+1}(v+1), \tag{19}$$

where the factor $v+1$ accounts for the dependence of the Raman cross section on the vibrational quantum number (see equation (5)).

As this approach relies heavily on the assumptions, that the lines can be viewed as non-interacting and χ_{NR}, $\mathrm{Re}(\chi_R) \ll \mathrm{Im}(\chi_R)$, which are certainly not valid for small admixtures of the probed gas species [37] and probably also not true for the weak signals of the higher vibrational states, in this work the population densities are extracted by fitting the full theoretical spectra to the measured ones.

To calculate the population differences in the susceptibility expression different models are used depending on the corresponding conditions. One possibility would be to assume that the vibrational states are Boltzmann distributed but with a different temperature than the rotational states like it was done for example by Messina *et al* [40]:

$$N(v,J) = \frac{g(J)}{Z} \mathrm{e}^{-\frac{E(v,J)-E(v,0)}{k_B T_{rot}}} \times \mathrm{e}^{-\frac{E(v,0)-E(0,0)}{k_B T_{vib}}} \tag{20}$$

with the partition function

$$Z = \sum_{v,J} g(J) \mathrm{e}^{-\frac{E(v,J)-E(v,0)}{k_B T_{rot}}} \times \mathrm{e}^{-\frac{E(v,0)-E(0,0)}{k_B T_{vib}}} \tag{21}$$

and $T_{vib} \neq T_{rot}$. Another approach would be the Treanor distribution assuming dominant V–V transfer collisions between the molecules:

$$N(v,J) = \frac{g(J)}{Z} \mathrm{e}^{-\frac{E(v,J)-E(v,0)}{k_B T_{rot}}} \times \mathrm{e}^{-\frac{v(E(1,0)-E(0,0))}{k_B T_{vib}}} \times \mathrm{e}^{-\frac{v(E(v,0)-E(1,0))}{k_B T_{rot}}} \tag{22}$$

with

$$Z = \sum_{v,J} g(J) \mathrm{e}^{-\frac{E(v,J)-E(v,0)}{k_B T_{rot}}} \times \mathrm{e}^{-\frac{v(E(1,0)-E(0,0))}{k_B T_{vib}}} \times \mathrm{e}^{-\frac{v(E(v,0)-E(1,0))}{k_B T_{rot}}}. \tag{23}$$

The degeneracy of the rotational states is given by

$$g(J) = \begin{cases} 6(2J+1), & \text{if } J \text{ even} \\ 3(2J+1), & \text{if } J \text{ odd.} \end{cases} \tag{24}$$

Both distributions assume a single vibrational temperature and are for the temperatures and relatively low vibrational states measured in this work essentially indistinguishable considering the uncertainty of the CARS measurements.

As in previous measurements of the ro-vibrational distribution [19–22], here, it was found that a single vibrational temperature is not sufficient to fully describe the vibrational distribution for $v > 3$. Therefore, here a distribution function considering two vibrational temperatures, a cold and a hot one, is introduced similar to the one used in [41]. The subtle difference compared to [41] is that the hot part of the distribution only includes states with $v \geq 1$. This is rooted in the interpretation that the hot distribution is made up by molecules which are excited during the current discharge cycle. The further motivation of this two-temperature distribution function (TTDF) is discussed in more detail in the companion paper [42] and here only the formula is given:

$$\begin{aligned} N(v,J;T_{rot},T_{vib,c},T_{vib,h},R_h) = g(J)\mathrm{e}^{-\frac{E(v,J)-E(v,0)}{k_B T_{rot}}} \\ \times \Bigg[\frac{1-R_h}{Z_c}\mathrm{e}^{-\frac{E(v,0)-E(0,0)}{k_B T_{vib,c}}} \\ \underbrace{+\frac{R_h}{Z_h}\mathrm{e}^{-\frac{E(v,0)-E(0,0)}{k_B T_{vib,h}}}}_{\text{for } v>0}\Bigg] \end{aligned} \tag{25}$$

with the partition function for the "cold" molecules

$$Z_c = \sum_{v,J} g(J) \mathrm{e}^{-\frac{E(v,J)-E(v,0)}{k_B T_{rot}}} \times \mathrm{e}^{-\frac{E(v,0)-E(0,0)}{k_B T_{vib,c}}} \tag{26}$$

and

$$Z_h = \sum_{v>0,J} g(J) \mathrm{e}^{-\frac{E(v,J)-E(v,0)}{k_B T_{rot}}} \times \mathrm{e}^{-\frac{E(v,0)-E(0,0)}{k_B T_{vib,h}}} \tag{27}$$

for the "hot" molecules.

The last condition investigated in this work is several microseconds after the discharge pulse. On this timescale the V–V collisions determine the temporal behavior and the two-temperature description is not valid anymore. Indeed, all of the distributions mentioned above fail in this regime. To make a distribution function independent analysis possible only the Q branch, $\Delta v = 1, \Delta J = 0$ is considered.

If the rotational states in a vibrational level v follow a Boltzmann distribution $f_v(J, T_{v,rot})$ with rotational temperature $T_{v,rot}$, the population difference for a given transition $(v \to v+1; J)$ is

$$\begin{aligned} \Delta N_{v,v+1;J} &= N_v f_v(J, T_{v,rot}) - N_{v+1} f_{v+1}(J, T_{v+1,rot}) \\ &\approx (N_v - N_{v+1}) f(J, T_{rot}) \\ &= \Delta N_{v,v+1} f(J, T_{rot}). \end{aligned} \tag{28}$$

Here, in the second step it is assumed that the rotational temperature in the different vibrational states is the same and that the vibrational corrections to the rotational distributions are negligible. In this way the fitting parameters concerning the vibrational states are reduced to $\Delta N_{v,v+1}$.

2.2. Benchmark

To benchmark our CARS code and the determination of vibrational temperatures from the fitting parameters several spec-

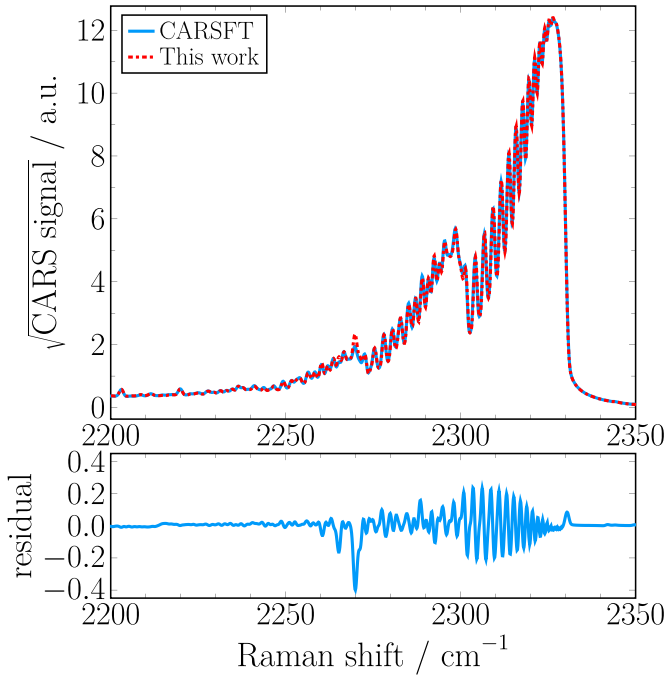

Figure 3. CARSFT [38] spectrum at $T = 2000$ K and fit by the code developed in this work with independent vibrational and rotational temperatures $T_{vib} = 2000$ K and $T_{rot} = 1996$ K.

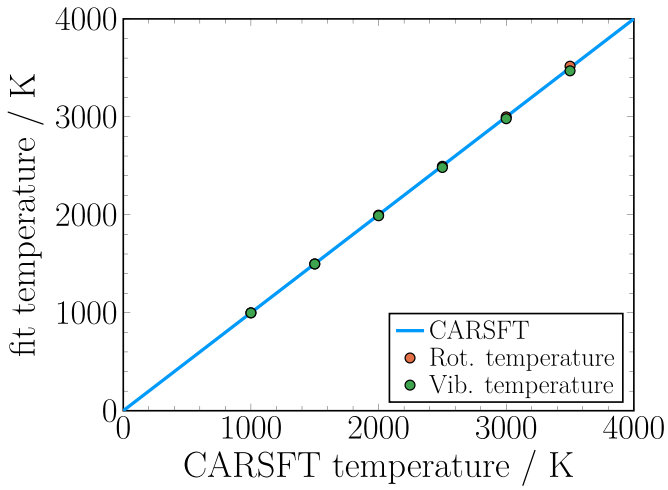

Figure 4. Comparison of the vibrational and rotational temperatures extracted by the fitting routine and the equilibrium temperatures used to produce the CARSFT spectra. The diagonal line corresponds to perfect agreement between theoretical and fitted temperatures.

tra are generated by the popular CARSFT code [38] with a spectral resolution similar to our experiments for thermal equilibrium conditions and evaluated by our fitting routines assuming Boltzmann distributed vibrational and rotational states where T_{rot} and T_{vib} are independent of each other. An example fit for an equilibrium temperature of 2000 K is shown in figure 3. In figure 4 the fitting results are shown for several spectra generated by the CARSFT code. The agreement for both the rotational and the vibrational temperature is very good over the whole range, and it is reasonable to assume that the code used in this work accurately describes real CARS spectra in the given temperature range even if $T_{rot} \neq T_{vib}$.

3. Electric field measurements

To understand the plasma processes leading to the measured ro-vibrational distributions knowledge about the electric field in the discharge is essential. To measure the electric field value in the discharge the electric field induced second harmonic (E-FISH) generation technique [43–52] is used. It is a third-order nonlinear process involving an electric field of a light wave with frequency ω (laser emission) and an external applied electric field, E. As a result, light with doubled frequency is generated with intensity proportional to E^2:

$$I^{(2\omega)} = kN^2 I_{\text{laser}}^2 E^2, \tag{29}$$

where k is a constant value depending on the gas mixture, its susceptibility and the optical system, N is the gas density and I_{laser} the laser pulse energy.

To obtain the absolute value of the electric field a calibration is necessary. Signal intensities at known electric field values are usually measured to determine the proportionality coefficient between $I^{(2\omega)}/I_{\text{laser}}^2$ and E^2. Without the plasma the electric field is Laplacian and depends only on the discharge cell geometry and the voltage applied to the electrodes. Taking the discharge cell configuration into account, see figure 10, it is assumed that the electric field is uniform in the vicinity of the measurement points and corresponds to the capacitor like configuration with $E = U/d$, where U is the applied voltage and $d = 1$ mm is the inter-electrode gap. It was shown [52] that if a DC voltage is used to provide the Laplacian field the slope of the calibration curve, $I^{(2\omega)}/I_{\text{laser}}^2$ vs. E^2, may be underestimated leading to an overestimation of the electric field in the discharge. It was proposed that the applied field is shielded by the charges generated due to tightly focused laser emission, thus the field is not Laplacian even without the discharge. If a DC voltage is applied, these charges are separated between the electrodes by the permanent electric field, drift to the electrodes and, thus, do not recombine forming an electric field, which shields the applied one. To avoid this problem it was proposed [52] to use nanosecond pulses at a low repetition rate instead of DC voltage. The same approach is used in this work. The calibration curve obtained with 150 ns pulses with sub-breakdown amplitude is presented in figure 5. It is clearly seen that the photomultiplier tube (PMT) signal normalized by the laser energy linearly depends on the square of the applied electric field in accordance with (29). The parameters of the fit are used to obtain the electric field value from the measured signal intensity during the discharge. It should be noted here, that the gas temperature—and therefore the particle density—is different in the discharge (see section 5) than in the calibration performed at room temperature, this has been taken into account.

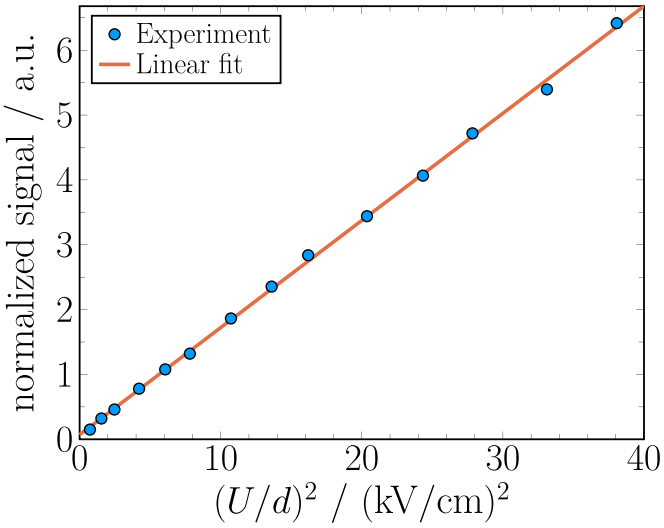

Figure 5. Calibration curve used for E-FISH measurements obtained with 150 ns rectangular pulses at 10 Hz: measured second harmonic intensity normalized by the laser energy as a function of square of applied Laplacian electric field strength (symbols) together with the linear fit (solid curve).

4. Experimental setup

The experimental setup used in this work consists of optical setups for the CARS and E-FISH measurements and the electrical setup of the plasma jet. The optical setups are synchronized with the discharge by a synchronization unit.

4.1. Optical setup for the CARS measurements

The optical setup—a modified version of the one used in [53] and [54] for CARS-based electric field measurements—is shown in figure 6. The second harmonic of an injection seeded Nd:YAG laser (532 nm, Continuum Powerlite Precision II 9020, 6 ns FWHM, 20 Hz repetition rate) is used both as pump laser for two dye lasers (Radiant Dyes Jaguar D90MA) and as pump beam in the CARS process. One of the dye lasers is a narrowband dye laser, which is used as probe beam. The laser emission at 560 nm is produced by a Rhodamine 6G dye solution and a spectral width of about 0.05 cm^{-1} is reached with a double grating configuration. Here, light with 560 nm was chosen for the probe beam to be able to perform CARS measurements in carbon dioxide and nitrogen simultaneously [55] at a later stage. In the broadband dye laser (BBDL) the double grating configuration for the wavelength selection is bypassed by a mirror to allow broadband operation. The desired spectrum of the BBDL—which is monitored by a broadband spectrometer—is reached by using a mixture of Pyrromethene 597 and Rhodamine B/101. Initially a mixture of Pyrromethene 597 and Pyrromethene 650 was used as in [56], but was found to drift to lower wavelengths too quickly. As an attempt to increase the lifetime of the mixture Pyrromethene 650 was replaced by the two Rhodamine dyes. To adjust the temporal overlap of the three laser beams two delay stages are used: One for the part of the Nd:YAG beam which is used in the CARS process and the other one for the pump beam of the BBDL. All three laser beams are first attenuated to pulse energies around 5 mJ and then focused to the probe volume by an achromatic lens with 50 cm focal length. A three-dimensional folded BOXCARS [57] geometry is used as depicted in figure 7. The CARS signal is produced only in the volume, where all three laser beams overlap. The spatial resolution perpendicular to the beam paths is therefore given by the smallest beam waist and should be in the order of 100 µm. To determine the spatial resolution along the beam path direction a glass plate of 1 mm thickness is scanned through the probe volume along the beam path. Due to its high density the glass plate generates a strong non-resonant CARS spectrum, when inserted in the probe volume. The spectrally integrated intensity generated this way is shown in figure 8 for different positions. An intensity profile with a full width at half maximum of slightly less than 5 mm is obtained, which will be assumed to be the spatial resolution in the following discussions. The anti-Stokes signal beam passes through a low pass filter to reduce stray light from the lasers and is guided to the CARS spectrometer (Jobin Yvon HR1000, 1800 lines mm^{-1} holographic grating) with a PCO edge 4.2LT sCMOS camera as detector. Furthermore, a photo diode is used to measure the time stamp of the laser on the oscilloscope, which also measures the current–voltage waveforms of the plasma jet. The trigger of the Nd:YAG laser, the spectrometers and the oscilloscope (Lecroy WaveSurfer 510) are synchronized by a synchronization unit to allow the accumulation of single shot measurements. Finally, all measured data are collected by a custom made DAQ software on the computer.

4.2. Optical setup for the field measurements

The emission of a Nd:YAG laser (EKSPLA SL234) at 1064 nm with a pulse duration of 100 ps is focused to the middle of the discharge gap by a lens with focal length of 200 mm. The light at the second harmonic (532 nm) generated in presence of the external field is separated from the fundamental harmonic by a dichroic mirror and detected by a PMT (Hamamatsu H11901-210) with laser line filter (Thorlabs FL532-1) installed at its entrance. For the schematic view and more detailed description of the experimental setup used for the measurements of the electric field, please see [52], where a discharge with the same geometry was investigated.

4.3. Electrical setup and discharge jet

The electrical setup of the plasma jet is depicted in figure 9.

A negative DC high voltage (Heinzinger LNC 6000-10neg) is applied to the input of a high voltage switch (Behlke HTS 81). In order to protect the switch and increase the discharge stability the current is limited to < 30 A by a 255 Ω series resistor between switch and cathode of the plasma jet. Additionally, a 2 kΩ resistor, installed in parallel to the discharge, ensures that residual charges are removed from the electrodes after each discharge pulse. The voltage at the cathode relative to ground is measured by a high voltage probe (Lecroy PPE6kV) and the current is measured between the anode and ground by a current probe (American Laser Systems, Model

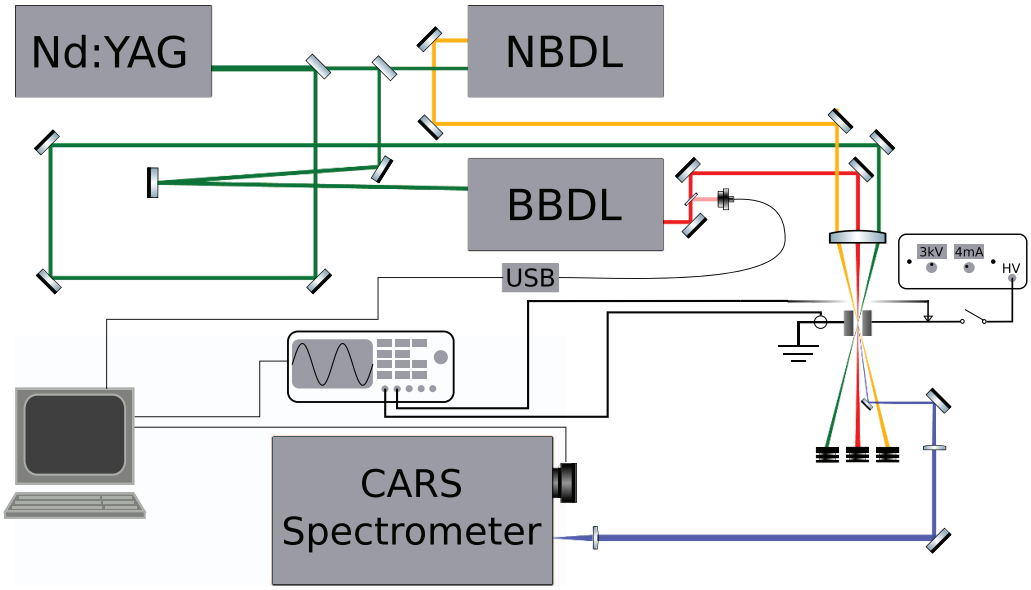

Figure 6. Optical setup of the CARS measurements. The broadband dye laser (BBDL) and the narrowband dye laser (NBDL) are both pumped by the injection seeded Nd:YAG laser. The spectrum of the BBDL is recorded during the measurements with a compact USB spectrometer (USB). Further information about the setup are given in the text.

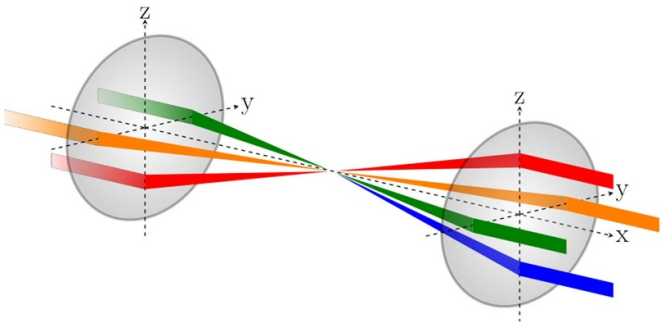

Figure 7. Three-dimensional phase matching in folded BOXCARS geometry. For technical reasons in this work only the blue anti-Stokes beam is collimated (see also figure 6).

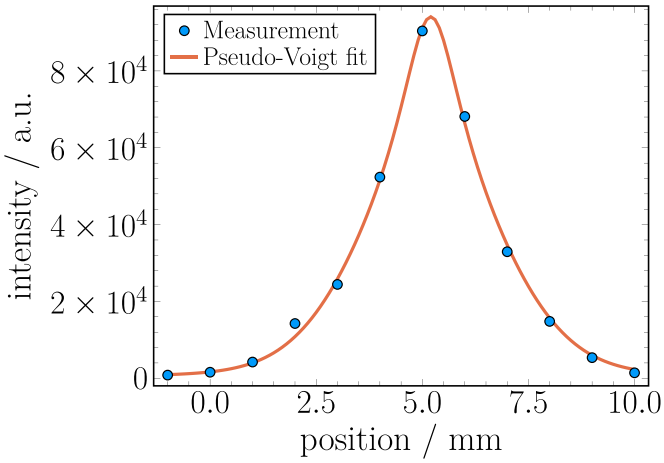

Figure 8. Non-resonant CARS intensity generated in a 1 mm thick glass plate. The position axis is defined along the laser beam paths (or equivalently along the discharge channel, see also figure 10). The intensity is the integrated spectral intensity, that is generated, when the glass plate is inserted into the beam paths at the corresponding position. The zero position is coincides with the gas inlet of the plasma jet introduced in the next section, while the exit of the jet is at 10 mm (compare also figure 10 for the position of the probe volume relative to the discharge).

711 Standard). The Behlke switch is triggered by a 1 kHz TTL signal which is synchronized to the 20 Hz trigger signal of the Nd:YAG laser through a frequency divider. The duration of the high voltage pulse can be controlled by the duration of the trigger pulses at a digital delay generator with a minimum pulse length of 150 ns.

The plasma jet itself consists of two plane parallel molybdenum electrodes with an area of 1 mm × 20 mm, which are positioned between two glass plates at a distance of 1 mm. Molybdenum is chosen as electrode material because of its relatively low sputter rate and the resulting longer lifetime of the electrodes. To allow operation in pure nitrogen at pressures around 200 mbar the electrode surfaces must be prepared carefully in order to avoid arcing. For this purpose the electrodes were polished with a final grit size of P2000.

To illustrate the gas flow the front and the side view of the jet are shown in figure 10. The gas enters the electrode gap through a hole in the lower glass plate and exits on both sides after being exposed to multiple discharge pulses due to the gas residence time. This design allows the laser beams to pass through the jet along the electrodes. It should be noted, that the measurement volume of the CARS setup is not in the center of the jet as there mostly unexcited gas would be measured, which was not exposed to the discharge yet. Instead, it is positioned between the gas inlet in the center and one of the exits (see figure 10).

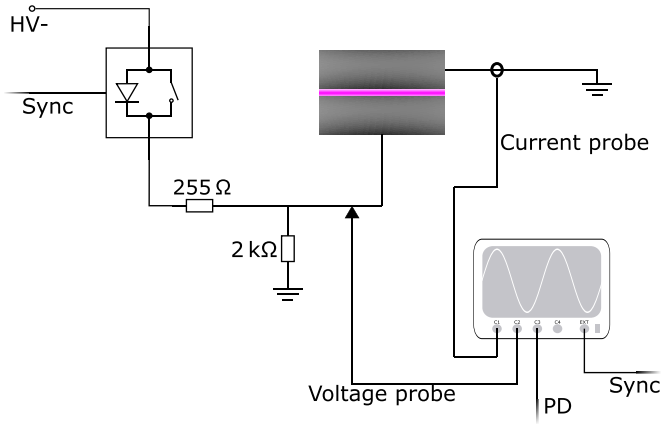

Figure 9. Electrical setup of the plasma jet.

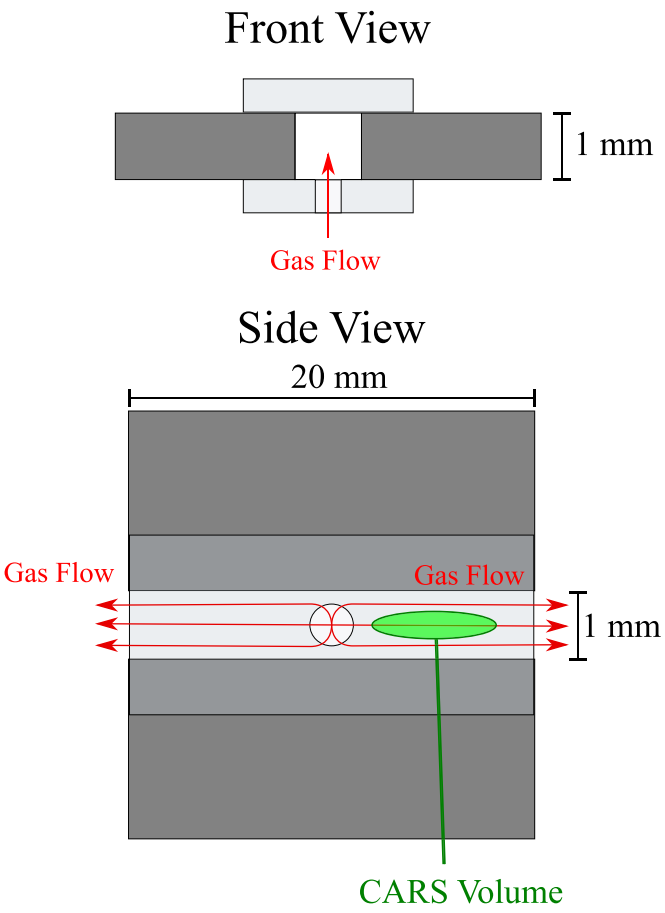

Figure 10. Front and side view of the discharge jet. The 1 mm gap between the electrodes is enclosed by two glass plates. One of the glass plates has a small borehole in the middle which serves as inlet for the gas flow. From the center of the discharge gap the gas is guided to the exits on both sides yielding two identical discharge channels with a cross section of 1 mm^2 and a length of 10 mm.

To ensure a controlled atmosphere the jet is enclosed in a discharge chamber which allows regulating the pressure and the gas flow through the jet.

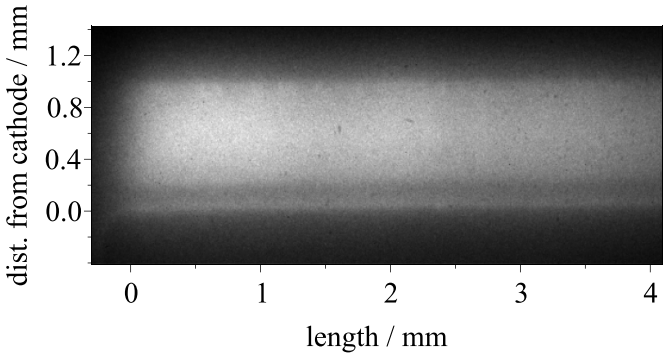

Figure 11. Single shot ICCD image from the side (i.e. side view in figure 10) with an exposure time of 300 ns. Due to the limited optical access of the chamber, only part of the discharge is shown. The high voltage pulses are applied to the lower electrode (as shown in figure 9).

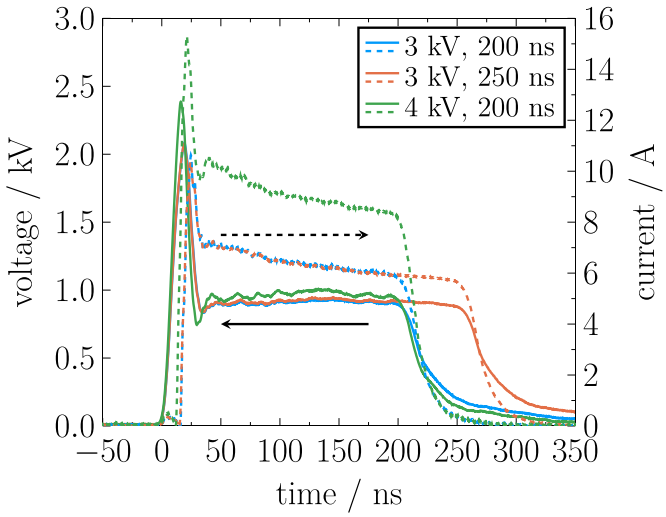

Figure 12. Voltage (solid lines) at the powered electrode and current (dashed lines) to ground during the discharge for the different applied voltage pulses. While the maximum peak voltage at the time of the breakdown increases for the higher applied voltage it can be noted that the voltage drop over the discharge gap during the following plateau is nearly the same for all three conditions. The current on the other hand is significantly higher for the 4 kV case.

An ICCD image of a single discharge pulse is shown in figure 11. No arcing is visible under the investigated discharge conditions and a relatively homogeneous discharge is achieved.

5. Results and discussion

Three time resolved measurements are performed in pure nitrogen discharges for three different voltage pulse forms. The other input parameters are fixed for all three measurements: The nitrogen flow is 20 sccm at a pressure of 200 mbar and the pulse repetition frequency is 1 kHz. The pulse waveforms are illustrated in figure 12 together with the resulting current waveforms.

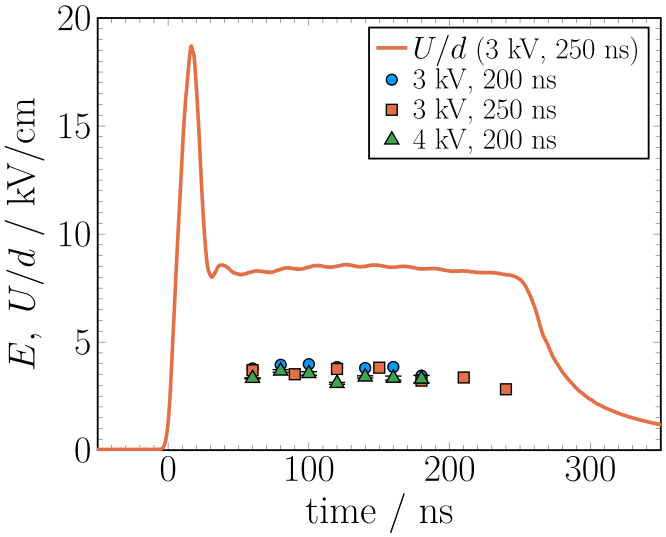

Figure 13. Electric field temporal development at 500 µm from the cathode measured by E-FISH technique (symbols) for different HV pulses compared with the electric field profile calculated as voltage over gap ratio for the 3 kV, 250 ns measurement (line). As the voltage amplitude during the plateau phase is quite similar for all three measurements (see figure 12) only one waveform is shown.

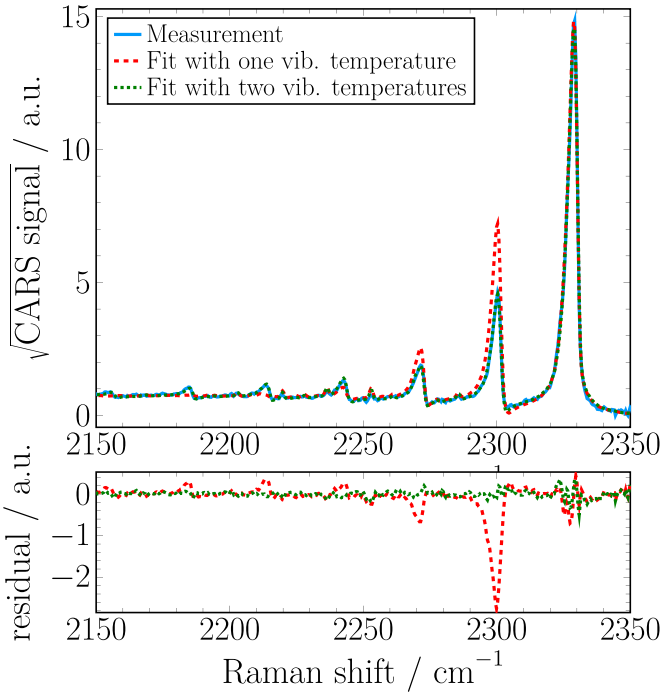

Figure 14. Comparison of a measured spectrum with theoretical spectra for Boltzmann distributed vibrational states with $T_{vib} = 1800$ K and for a two-temperature distribution with $T_{vib,c} \approx 1200$ K and $T_{vib,h} \approx 5200$ K. The spectrum corresponds to $t = 300$ ns in the measurement set for an applied voltage of 4 kV (approx. 50 ns after the pulse).

In the following the different measurements will be referred to by the voltage applied by the DC high voltage generator (which is not the same as the measured amplitude voltages at the electrodes) and the pulse duration.

The CARS spectra in this work are averaged over 1000 laser shots, before they are evaluated by the fitting code.

First the results during the discharge pulse will be discussed and afterwards the dynamics during the afterglow will be presented.

5.1. Discharge phase

The electric field during the current plateau is shown in figure 13 for different DC voltages used to feed the high voltage switch and different HV pulse durations. The electric field has a constant value of ≈ 3.5 kV cm^{-1} or ≈ 81 Td during the plateau, which is about the same for the different pulse durations. Moreover, the electric field amplitude only very weakly depends on the DC voltage as well. Despite the different DC voltage, after the breakdown the cathode voltage is about the same, see figure 12. This can be explained by a higher electron density generated during the breakdown at the higher DC voltage leading to a higher electric current and consequently a higher voltage drop at the series resistor. According to calculations with Bolsig+ [58] using the IST-Lisbon data set [59] the measured field corresponds to a mean electron energy of 1.8 eV or an electron temperature of $T_e = 1.2$ eV.

To demonstrate the necessity of the TTDF (25) for the CARS fitting routine, in figure 14 a measured spectrum with its corresponding TTDF fit is compared with a theoretical spectrum for a single vibrational temperature. From the figure it is obvious, that a single vibrational temperature

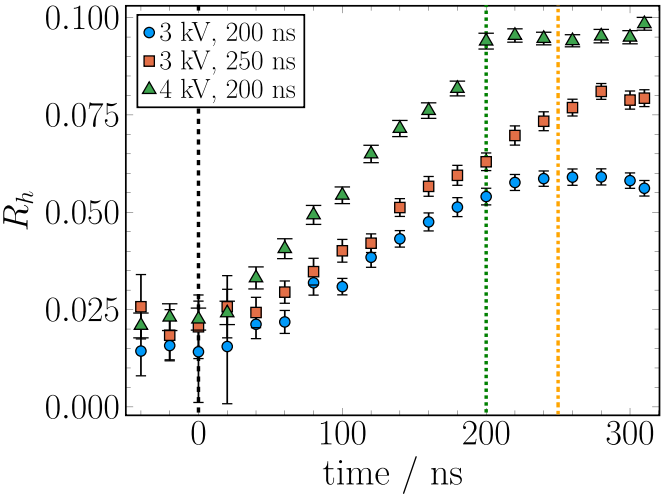

Figure 15. Time development of the fraction of vibrationally hot molecules R_h in (25). As guide for the eye the starting point of the voltage pulses is marked by the black dashed line and the end points of the 200 and 250 ns pulses are marked with the green and the orange dashed lines respectively. The uncertainties of R_h are determined from the local Jacobian of the best fit.

will not be able to reproduce the measured spectra during or shortly after the discharge. During the discharge pulse the full spectrum—consisting of O- and Q-branch transitions in the observed wavelength region—is fitted while assuming a two-temperature distribution according to (25). The results for the fitting parameters R_h and $T_{vib,h}$ are shown in figures 15 and 16

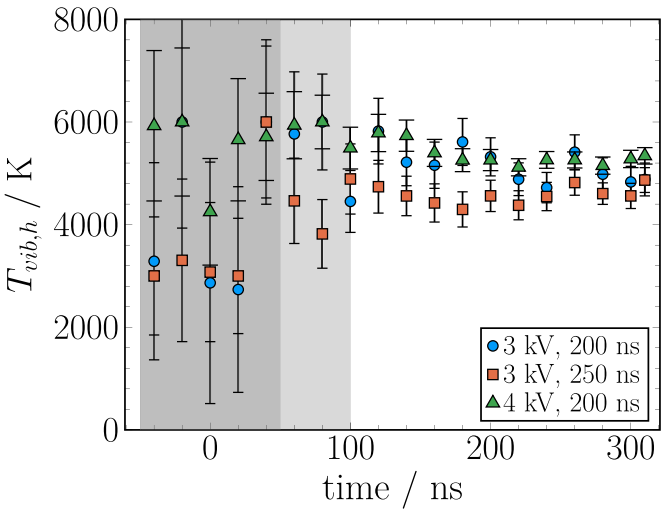

Figure 16. Time development of the temperature of the vibrationally hot molecules $T_{vib,h}$ in (25). The gray areas are used to emphasize that temperatures for times lower than 50 ns (4 kV) or 100 ns (3 kV) are not reliable for physical interpretation (see text). The uncertainties of $T_{vib,h}$ are determined from the local Jacobian of the best fit.

respectively. The uncertainties of the fitting parameters are determined from the local Jacobian of the corresponding best fit solutions. During the discharge pulse the fraction of vibrationally hot molecules, R_h, increases linearly. This agrees well with the essentially constant current and electric field after the ignition—suggesting constant excitation conditions during the whole discharge pulse. It is clearly visible, that the slope of R_h is the highest for the pulse with the higher current amplitude (4 kV applied DC voltage) while the two measurements with 3 kV applied voltage share a lower slope and differ only by a small offset due to different initial conditions. Those initial conditions (weighted average over the first three data points) are 0.015 ± 0.003 (3 kV, 200 ns), 0.021 ± 0.004 (3 kV, 250 ns) and 0.022 ± 0.002 (4 kV, 200 ns). As the electric field is the same in all three cases, the difference in slope should be mainly caused by a higher electron density in the 4 kV case. A more detailed discussion of the slope, $\dot{R}_h$, is given in the companion paper [42]. The fact, that one of the measurements is performed with a longer pulse duration, is also reflected in figure 15 by a longer rise time of R_h (note the two vertical lines at about 200 and 250 ns marking the corresponding ends of the pulses).

In regard to the temperature of the hot population it has to be noted that the values at the beginning, when the amount of excited molecules is small, are not reliable or suitable for a direct interpretation. Firstly, at these times only states up to $v = 3$ can be detected as the densities of the other states are below the detection limit. Secondly, (25) is proposed to analyze the characteristics of the newly excited molecules (for further details the reader is referred to the companion paper [42]). Before the discharge pulse there are no 'newly' excited molecules yet and the non-zero value of the fitting parameter R_h only accounts for the small deviation from a normal Boltzmann distribution remaining from the previous voltage pulse still visible in the excited states $v = 1 - 3$. Therefore $T_{vib,h}$ suffers a large uncertainty, as it strongly depends on the higher states, which are not detected. So, to be able to use the two-temperature distribution in its original intent the newly excited molecules need to overtake the remaining deviation from a Boltzmann distribution. The criterion used here and in [42] is that R_h needs to at least surpass two times the average value of the data points before the ignition, so that the majority of the molecules belonging to the hot distribution consists of molecules excited during the current discharge pulse. The data points which are excluded from further discussion by the mentioned criterion are marked by a gray background in figure 16. Please note, that this criterion agrees quite well with the uncertainties of $T_{vib,h}$. Considering the previous remarks it stands out that $T_{vib,h}$ stays constant for all three measurements in the usable range. While the 200 ns-pulse measurements for 3 kV with 5200 ± 300 K (averaged over all data points with $t > 100$ ns) and the one for 4 kV with 5300 ± 200 K (average for $t > 50$ ns) are very close to each other, the measurement for the 250 ns pulse deviates with 4600 ± 200 K (average for $t > 100$ ns). This deviation is probably caused by a worse signal-to-noise ratio during that particular measurement set. The dye mixture of the broadband Stokes laser needs to be refreshed between measurement sets and while the spectrum of the Stokes beam is included in the calculation of the CARS spectra, the fluctuations of the Stokes beam result in different signal-to-noise ratios in the measured CARS signals for the different measurement sets. As this mainly affects the higher vibrational states due to their weaker signal, the effect is stronger on the fitting parameter influenced by those states, namely the hot vibrational temperature $T_{vib,h}$. In these cases, a small shift of the baseline could induce a systematic shift of the temperature, which is not necessarily reflected in the uncertainty determined from the local Jacobian. R_h on the other hand corresponds to the total amount of newly excited molecules and as the higher vibrational states only contribute by a small number—even at temperatures around 5000 K—the effect is small. This explains why there is no deviation from the expected behavior visible in figure 15. As one would expect the rotational temperature stays constant on time scales of the discharge with about $T_{rot} = 330 \pm 8$ K (mean value and standard deviation over all three measurement sets). Likewise, the vibrational temperatures of the cold bulk molecules stays nearly constant during the discharge pulse as well, but differ slightly for the different measurement sets. The two measurements with 3 kV applied DC voltage are quite close to each other with 1190 ± 40 K (200 ns pulse) and 1180 ± 40 K (250 ns pulse). For the 4 kV case the vibrational background temperature is slightly higher with 1300 ± 50 K.

As the densities of the vibrationally excited states are known from the fits, the gain of vibrational energy in the plasma volume during one discharge pulse can be calculated relative to the average energy of the first three measurement points (see figure 17).

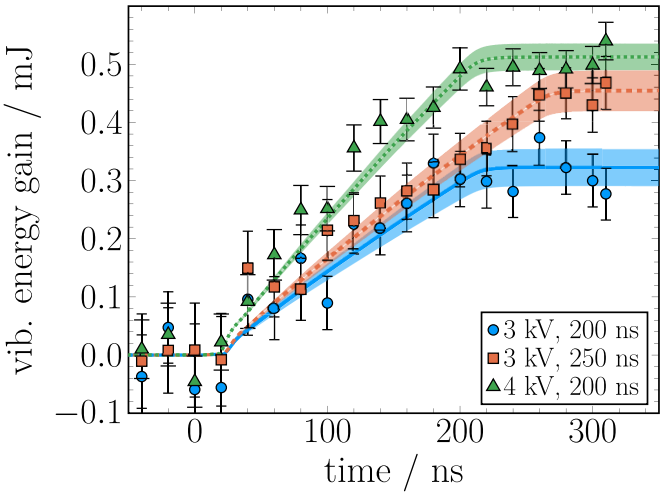

Figure 17. Gain of vibrational energy during the discharge pulse (symbols). The solid lines refer to the scaled total electrical energy coupled into the plasma obtained from the voltage and current waveforms in figure 12. The corresponding scaling factors are obtained from fitting to the measured vibrational energy gain and the uncertainty is visualized by the shaded area around the curve. The factors are found to be 0.27 ± 0.03 for 3 kV, 200 ns, 0.309 ± 0.024 for 3 kV, 250 ns and 0.287 ± 0.013 for 4 kV, 200 ns and describe the efficiency of the energy coupling into the vibrational degree of freedom (see text).

The energy deposited into the plasma up to the time t can be calculated from the measured voltage, $U(t)$, and current, $I(t)$, waveforms in figure 12 via

$$\mathcal{E}(t) = \int_{t_0}^{t} U(\tilde{t}) I(\tilde{t}) d\tilde{t}, \tag{30}$$

where t_0 is some point in time before the discharge pulse. The efficiency of the energy coupling into vibrational degrees of freedom is determined by multiplying (30) with a scaling factor. The scaled deposited energy is then fitted to the measured vibrational energy gain with the scaling factor as the only free fit parameter. The resulting factors for the three measurements are: 0.27 ± 0.03 for 3 kV, 200 ns, 0.309 ± 0.024 for 3 kV, 250 ns and 0.287 ± 0.013 for 4 kV, 200 ns. Please note, that the baseline for the vib. energy gain in figure 17 is given by the average of the first three data points (i.e. the data points before the ignition of the plasma). This introduces an uncertainty in the baseline which is not included fully in the above values of the uncertainties of the three scaling factors. It can be concluded that for all three measurements about 30% of the deposited energy is coupled into vibrational excitation each pulse. The fact that the efficiency does not vary significantly between the three conditions can be explained by the electric field, which is essentially the same for all pulse shapes. This value of 30% agrees well with the one reported by Montello *et al* [22] and Deviatov *et al* [20]. Another remarkable aspect in regard to the energy efficiency of the vibrational excitation can be found through a comparison with the energy dissipated in the bulk. With an electric field of 3.5 kV cm^{-1} and a bulk length of roughly 1 mm one obtains a voltage drop over the bulk of 350 V. During the plateau period the voltage over the discharge gap is around 1 kV for all investigated cases. Because the current is the same everywhere in the discharge gap, the power dissipated in the bulk accounts for 35% of the total discharge power (during the quasi-DC plateau period), while the remaining energy will be dissipated in the high field of the cathode sheath. Therefore, it can be concluded, that most of the energy dissipated in the bulk is transferred into vibrational excitation. The previous statement relies on the assumption, that there is no significant vibrational excitation in the cathode sheath. This is justified by the necessarily high electric field in the sheath, which is much more favorable for electronic excitation and ionization than for vibrational excitation.

5.2. Afterglow

In the period between two pulses (25) is not suitable to describe the VDF of the nitrogen molecules, because interaction between the bulk and the excited molecules makes it difficult to distinguish effects on the fitting parameters R_h and $T_{vib,h}$. Furthermore, it is not given, that the hot molecules—if this definition can still be applied—follow a distribution which can be approximated by a Boltzmann distribution. For this reason the Q-branch-only fitting scheme discussed in the end of section 2.1 is used, which yields the population differences between two neighboring vibrational states (here normalized to the total particle density of nitrogen) $\frac{N_v - N_{v+1}}{N_{gas}}$ as output parameters by considering only the Q branch transitions. The population differences $\Delta N_v = N_v - N_{v+1}$—in the following ΔN_v is always assumed to be in arbitrary units—obtained by the fit could now be processed further by either making assumptions on the population difference between the ground and the first excited state [18] or by setting the population of the upper state for the highest detectable transition to zero [22]: $\Delta N_{v_{\max}} = N_{v_{\max}} - N_{v_{\max}+1} \approx N_{v_{\max}}$. With $v_{\max}$ as starting point the population densities can then simply be obtained by $N_v = N_{v+1} + \Delta N_v$. Finally, they are normalized to $\sum_v N_v$ effectively yielding the fraction of molecules in state v compared to the gas density. Obviously, the assumption $N_{v_{\max}} \approx 0$ introduces a certain error into the analysis. To estimate this error one may take a look at the ratio of two neighboring states following a Boltzmann distribution $N_{v+1}/N_v \approx \exp\left(-\frac{\hbar\omega_e}{k_B T_{vib}}\right)$ (neglecting the anharmonicity for simplicity). At room temperature this ratio is indeed much smaller than unity and the above approximation is valid. But as it was shown in the previous section that the highest vibrational states can have a temperature of about 5000 K leading to $N_{v+1}/N_v \approx 0.5$. Here the approximation is clearly not valid anymore. Therefore, in this work $N_{v_{\max}+1}$ is extrapolated from $N_{v_{\max}}$ so that one obtains for the population difference

$$\begin{aligned}\Delta N_{v_{\max}} &\approx N_{v_{\max}} - N_{v_{\max}} \exp\left(-\frac{E_{v_{\max}+1} - E_{v_{\max}}}{k_B \tilde{T}_{vib}}\right) \\ &\approx N_{v_{\max}} \left[1 - \exp\left(-\frac{E_{v_{\max}+1} - E_{v_{\max}}}{k_B \tilde{T}_{vib}}\right)\right]\end{aligned} \tag{31}$$

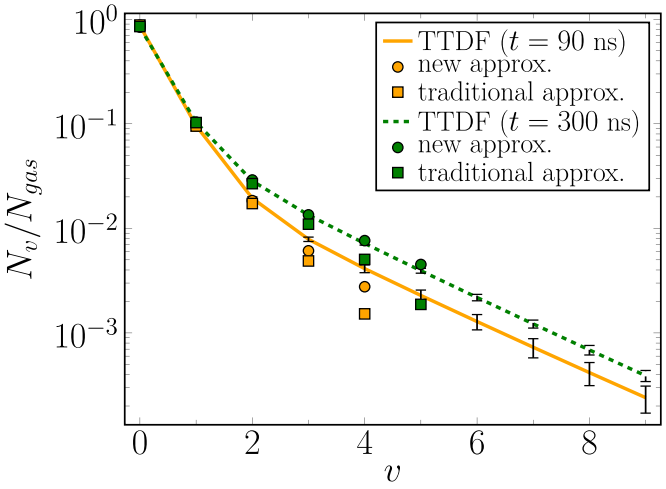

Figure 18. Comparison of the population densities obtained by the two-temperature distribution and the Q-branch-only fit with the two different evaluation methods. The solid and dashed lines correspond to the TTDF at different points in time, $t = 90$ ns and $t = 290$ ns respectively. The symbols in the corresponding colors denote the results at the same times from the Q-branch-only fits evaluated with the newly proposed method (circles) and the traditional one (squares).

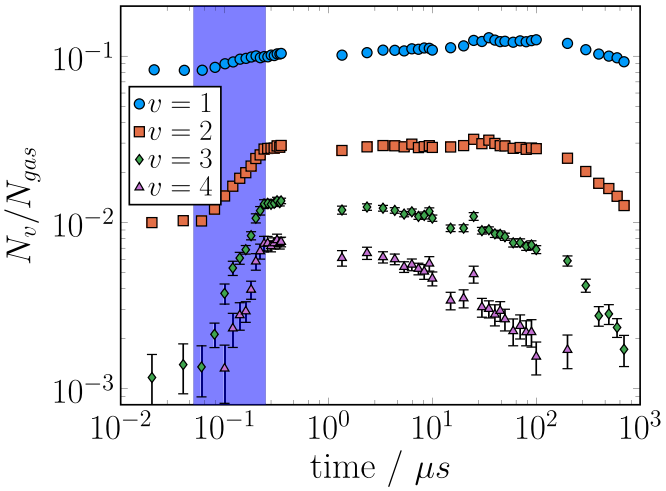

Figure 19. Relative population densities for $v = 1, 2, 3, 4$ during the discharge and in the afterglow for 4 kV applied DC voltage and 200 ns pulses. The blue area marks the time of the discharge pulse.

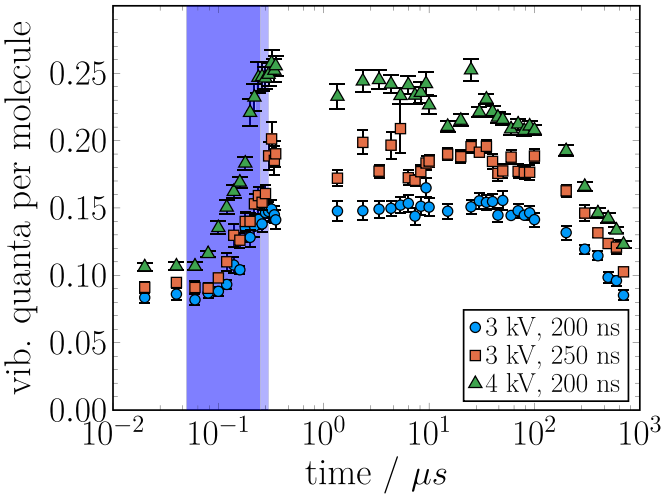

Figure 20. Vibrational quanta per molecule for all three measurements. The blue rectangles mark the on-time of the discharge pulse with 200 ns (dark shaded) and 250 ns (light shaded).

where $\tilde{T}_{vib}$ is estimated from the ratio of the two highest measured population differences:

$$\tilde{T}_{vib} \approx -\frac{E_{v_{\max}} - E_{v_{\max}-1}}{k_B \ln \frac{\Delta N_{v_{\max}}}{\Delta N_{v_{\max}-1}}}. \tag{32}$$

In figure 18 our approximation (31) is compared with the traditional approximation $N_{v_{\max}} \approx 0$ and the full TTDF fit from the previous section for two different points in time when the TTDF is assumed to be valid—during the discharge and shortly after. As can be seen quite clearly the agreement between the new method and the TTDF is significantly better than for the traditional approach. The small residual deviation at $t = 90$ ns is probably caused by the effect of the 'bend' of the distribution function between the cold and the hot parts on the estimation of $\tilde{T}_{vib}$ in (32)—leading to a slight underestimation of $\tilde{T}_{vib}$. It should be stressed, that while an underestimation of $N_{v_{\max}}$ by a factor of about 2 in the approximation $\Delta N_{v_{\max}} \approx 0$ might be considered acceptable under some conditions, this error amplifies when the data are used to extrapolate to higher vibrational states. Therefore, (31) and (32) are used in this work for the CARS spectra in the afterglow where the shape of the distribution function is not known *a priori*.

In figure 19 the relative population densities from the states 1 up to 4 are shown for the measurement with 4 kV applied DC voltage. While the population of the first vibrational state increases and the one of the second stays approximately constant, the higher states decrease on timescales smaller than about 100 µs. These dynamics can be attributed to V–V transfer between the molecules [42]. The general decrease of all excited states on longer timescales was found to be mainly due to deactivation at the walls [42]. As one can already guess from figure 19 the number of vibrational quanta does not seem to increase in the afterglow due to deexcitation of electronically excited molecules as it was observed by other groups in their discharges [22]. This is shown explicitly for all three measurement sets in figure 20. The number of vibrational quanta per molecule stays approximately constant during the V–V transfer phase and finally decreases to its original value due to losses at the walls with reasonable decay times [42].

6. Conclusions

In this work, a plasma is generated by applying high voltage pulses of 200 and 250 ns duration to plane parallel molybdenum electrodes in nitrogen at 200 mbar. In contrast to DBD discharges, more commonly used at these pressures, the metal electrodes allow for a nearly constant conduction current after

the ignition phase of the plasma until the end of the pulse. The electric field in these conduction current plateaus is measured by the E-FISH method and found to be constant during the discharge with a value around 81 Td for all conditions investigated here. These constant discharge conditions were previously observed in hydrogen plasmas (otherwise similar discharge conditions as in this work) both in simulations and measurements [53, 60–62]. CARS spectra were measured for three different high voltage pulses. To extract information from those spectra, which are more reliable than those from a simple analysis of the separate peak intensities in the CARS spectrum, a fitting routine is developed—motivated by existing CARS fitting routines for combustion systems in thermal equilibrium [27, 36, 38] and benchmarked against the popular CARSFT Fortran77 code [38]. Our fitting procedure allows for arbitrary VDFs to account for different conditions during the discharge phase and in the afterglow. It was found, that the vibrational excitation during the discharge phase can be described by a two-temperature distribution function consisting of a cold bulk with a near-equilibrium temperature $T_{vib,c} \approx 1300\ \mathrm{K} > T_{rot}$ making up the majority of the molecules and a hot part accounting for the molecules which are excited during the discharge pulse. The fraction of hot particles R_h increases close to linearly with time and the hot temperature $T_{vib,h}$ stays constant. This indicates constant excitation conditions during the pulses and agrees well with the constant electric field obtained by the E-FISH measurements and the quasi constant currents after the ignition phase (see figure 12) both implying a constant electron density. The constant plasma conditions allow a simple analysis of the energy efficiency of the vibrational excitation with the result, that around 30% of the dissipated energy in the discharge is transferred into the vibrational degree of freedom. This is close to the total energy estimated to be dissipated in the bulk region of the plasma. Additionally, the nearly constant plasma conditions allow an easy analysis of the vibrational dynamics and a comparison with corresponding constants in the literature. These are performed in a companion paper [42] and the reader is referred to there for more details. It can be summarized, that CARS is a complicated but powerful technique for measuring vibrational distribution functions in plasmas. Especially, the possibility to measure multiple species at once with the same experimental setup will prove extremely useful for investigating the influence of vibrational excitation on chemical and catalytic processes. These prospects will be investigated in future works with the same setup as introduced here.

Additionally, the application of CARS to an excited medium like a plasma itself provides access to further open research questions and opportunity for investigation. For example, the long living excited states in a plasma might influence the non-resonant susceptibility depending on the amount of excited species as it was observed for third harmonic generation in a pre-excited gas [63]. While the non-resonant part of the susceptibility is often ignored, it can be important for higher vibrational states where the resonant and non-resonant parts are of comparable amplitude.

Data availability statement

The data that support the findings of this study are available upon reasonable request from the authors.

Acknowledgments

This project is supported by the DFG (German Science Foundation) within the framework of the CRC (Collaborative Research Centre) 1316 'Transient atmospheric plasmas—from plasmas to liquids to solids'. Furthermore, the authors would like to thank Igor Adamovich, Kraig Frederickson and Ilya Gulko for sharing the CARSFT code and providing insights about the analysis of CARS spectra.

ORCID iDs

J Kuhfeld https://orcid.org/0000-0003-2335-2634
N D Lepikhin https://orcid.org/0000-0002-4027-5792
U Czarnetzki https://orcid.org/0000-0002-5823-1501

References

[1] Starikovskaia S M 2006 Plasma assisted ignition and combustion *J. Phys. D: Appl. Phys.* **39** R265–99
[2] Adamovich I V *et al* 2009 Plasma assisted ignition and high-speed flow control: non-thermal and thermal effects *Plasma Sources Sci. Technol.* **18** 034018
[3] Neyts E C and Bogaerts A 2014 Understanding plasma catalysis through modelling and simulation—a review *J. Phys. D: Appl. Phys.* **47** 224010
[4] Neyts E C, Ostrikov K K, Sunkara M K and Bogaerts A 2015 Plasma catalysis: synergistic effects at the nanoscale *Chem. Rev.* **115** 13408–46
[5] Whitehead J C 2016 Plasma–catalysis: the known knowns, the known unknowns and the unknown unknowns *J. Phys. D: Appl. Phys.* **49** 243001
[6] Stewig C, Schüttler S, Urbanietz T, Böke M and von Keudell A 2020 Excitation and dissociation of CO_2 heavily diluted in noble gas atmospheric pressure plasma *J. Phys. D: Appl. Phys.* **53** 125205
[7] Fridman G, Friedman G, Gutsol A, Shekhter A B, Vasilets V N and Fridman A 2008 Applied plasma medicine *Plasma Process. Polym.* **5** 503–33
[8] Stoffels E, Sakiyama Y and Graves D B 2008 Cold atmospheric plasma: charged species and their interactions with cells and tissues *IEEE Trans. Plasma Sci.* **36** 1441–57
[9] Kong M G, Kroesen G, Morfill G, Nosenko T, Shimizu T, Dijk J v and Zimmermann J L 2009 Plasma medicine: an introductory review *New J. Phys.* **11** 115012
[10] Graves D B 2012 The emerging role of reactive oxygen and nitrogen species in redox biology and some implications for plasma applications to medicine and biology *J. Phys. D: Appl. Phys.* **45** 263001
[11] Fridman A A 2008 *Plasma Chemistry* 1st edn (Cambridge: Cambridge University Press)
[12] Urbanietz T, Böke M, Schulz-von der Gathen V and von Keudell A 2018 Non-equilibrium excitation of CO_2 in an atmospheric pressure helium plasma jet *J. Phys. D: Appl. Phys.* **51** 345202

[13] Aerts R, Martens T and Bogaerts A 2012 Influence of vibrational states on CO_2 splitting by dielectric barrier discharges *J. Phys. Chem.* C **116** 23257–73

[14] Aerts R, Somers W and Bogaerts A 2015 Carbon dioxide splitting in a dielectric barrier discharge plasma: a combined experimental and computational study *ChemSusChem* **8** 702–16

[15] Bogaerts A, Kozák T, van Laer K and Snoeckx R 2015 Plasma-based conversion of CO_2: current status and future challenges *Faraday Discuss.* **183** 217–32

[16] Klarenaar B L M, Engeln R, Bekerom D C M v d, Sanden M C M v d, Morillo-Candas A S and Guaitella O 2017 Time evolution of vibrational temperatures in a CO_2 glow discharge measured with infrared absorption spectroscopy *Plasma Sources Sci. Technol.* **26** 115008

[17] Lempert W R and Adamovich I V 2014 Coherent anti-Stokes Raman scattering and spontaneous Raman scattering diagnostics of nonequilibrium plasmas and flows *J. Phys. D: Appl. Phys.* **47** 433001

[18] Shaub W M, Nibler J W and Harvey A B 1977 Direct determination of non-Boltzmann vibrational level populations in electric discharges by CARS *J. Chem. Phys.* **67** 1883–6

[19] Valyanskiĭ S I, Vereschagin K A, Vernke V, Volkov A Y, Pashinin P P, Smirnov V V, Fabelinskiĭ V I and Chapovskiĭ P L 1984 Studies of the kinetics of the vibrational and rotational distribution functions of nitrogen excited by a pulsed discharge *Sov. J. Quantum Electron.* **14** 1226

[20] Deviatov A A, Dolenko S A, Rakhimov A T, Rakhimova T V and Roi N N 1986 Investigation of kinetic processes in molecular nitrogen by the CARS technique *Zh. Eksp. Teor. Fiz.* **90** 429–36

[21] Vereshchagin K A, Smirnov V V and Shakhatov V A 1997 CARS study of the vibrational kinetics of nitrogen molecules in the burning and afterglow stages of a pulsed discharge *Tech. Phys.* **42** 487–94

[22] Montello A, Yin Z, Burnette D, Adamovich I V and Lempert W R 2013 Picosecond CARS measurements of nitrogen vibrational loading and rotational/translational temperature in non-equilibrium discharges *J. Phys. D: Appl. Phys.* **46** 464002

[23] Yang W, Zhou Q and Dong Z 2016 Simulation study on nitrogen vibrational kinetics in a single nanosecond pulse high voltage air discharge *AIP Adv.* **6** 055209

[24] Gatti N, Ponduri S, Peeters F J J, van den Bekerom D C M , Minea T, Tosi P, van de Sanden M C M and van Rooij G J 2018 Preferential vibrational excitation in microwave nitrogen plasma assessed by Raman scattering *Plasma Sources Sci. Technol.* **27** 055006

[25] Van Alphen S, Vermeiren V, Butterworth T, van den Bekerom D C M, van Rooij G J and Bogaerts A 2020 Power pulsing to maximize vibrational excitation efficiency in N_2 microwave plasma: a combined experimental and computational study *J. Phys. Chem.* C **124** 1765–79

[26] Schregel C G, Carbone E A D, Luggenhölscher D and Czarnetzki U 2016 Ignition and afterglow dynamics of a high pressure nanosecond pulsed helium micro-discharge: I. electron, Rydberg molecules and He (23S) densities *Plasma Sources Sci. Technol.* **25** 054003

[27] Farrow R L, Mattern P L and Rahn L A 1982 Comparison between CARS and corrected thermocouple temperature measurements in a diffusion flame *Appl. Opt.* **21** 3119–25

[28] Druet S A J and Taran J P E 1981 CARS spectroscopy *Prog. Quantum Electron.* **7** 1–72

[29] Eesley G L 1979 Coherent Raman spectroscopy *J. Quant. Spectrosc. Radiat. Transfer* **22** 507–76

[30] El-Diasty F 2011 Coherent anti-Stokes Raman scattering: spectroscopy and microscopy *Vib. Spectrosc.* **55** 1–37

[31] Marowsky G and Smirnov V V 1992 *Coherent Raman Spectroscopy: Recent Advances* (Berlin: Springer)

[32] Szymanski H A 1970 *Raman Spectroscopy: Theory and Practice* vol 2 (Berlin: Springer) (https://doi.org/10.1007/978-1-4684-3027-1)

[33] Lavorel B, Millot G, Lefebvre M and Péalat M 1988 Dunham coefficients of $^{14}N_2$ from CARS measurements of high vibrational states in a low-pressure discharge *J. Raman Spectrosc.* **19** 375–8

[34] Gilson T R, Beattie I R, Black J D, Greenhalgh D A and Jenny S N 1980 Redetermination of some of the spectroscopic constants of the electronic ground state of di-nitrogen $^{14}N_2$, $^{14}N^{15}N$ and $^{15}N_2$ using coherent anti-Stokes Raman spectroscopy *J. Raman Spectrosc.* **9** 361–8

[35] Huber K P and Herzberg G 1979 *Molecular Spectra and Molecular Structure: IV. Constants of Diatomic Molecules* (Berlin: Springer) (https://doi.org/10.1007/978-1-4757-0961-2)

[36] Luthe J C, Beiting E J and Yueh F Y 1986 Algorithms for calculating coherent anti-Stokes Raman spectra: application to several small molecules *Comput. Phys. Commun.* **42** 73–92

[37] Clark R J H and Hester R E (eds) 1988 *Advances in Non-Linear Spectroscopy* (*Advances in Spectroscopy*) vol 15 (Chichester: Wiley)

[38] Palmer R E 1989 *The Carsft Computer Code for Calculating Coherent Anti-Stokes Raman Spectra: User and Programmer Information* (Livermore, CA: SAND89-8206, Sandia National Labs)

[39] Hall R J, Verdieck J F and Eckbreth A C 1980 Pressure-induced narrowing of the cars spectrum of N_2 *Opt. Commun.* **35** 69–75

[40] Messina D, Attal-Trétout B and Grisch F 2007 Study of a non-equilibrium pulsed nanosecond discharge at atmospheric pressure using coherent anti-Stokes Raman scattering *Proc. Combustion Institute* vol 31 pp 825–32

[41] Du Y, Nayak G, Oinuma G, Ding Y, Peng Z and Bruggeman P J 2017 Emission considering self-absorption of OH to simultaneously obtain the OH density and gas temperature: validation, non-equilibrium effects and limitations *Plasma Sources Sci. Technol.* **26** 095007

[42] Kuhfeld J, Luggenhölscher D and Czarnetzki U 2021 Vibrational CARS measurements in a near-atmospheric pressure plasma jet in nitrogen: II. Analysis *J. Phys. D: Appl. Phys.* **54** 305205

[43] Dogariu A, Goldberg B M, O'Byrne S and Miles R B 2017 Species-independent femtosecond localized electric field measurement *Phys. Rev. Appl.* **7** 024024

[44] Goldberg B M, Chng T L, Dogariu A and Miles R B 2018 Electric field measurements in a near atmospheric pressure nanosecond pulse discharge with picosecond electric field induced second harmonic generation *Appl. Phys. Lett.* **112** 064102

[45] Simeni Simeni M, Tang Y, Hung Y C, Eckert Z, Frederickson K and Adamovich I V 2018 Electric field in Ns pulse and AC electric discharges in a hydrogen diffusion flame *Combust. Flame* **197** 254–64

[46] Simeni M S, Tang Y, Frederickson K and Adamovich I V 2018 Electric field distribution in a surface plasma flow actuator powered by ns discharge pulse trains *Plasma Sources Sci. Technol.* **27** 104001

[47] Chng T L, Brisset A, Jeanney P, Starikovskaia S M, Adamovich I V and Tardiveau P 2019 Electric field evolution in a diffuse ionization wave nanosecond pulse discharge in atmospheric pressure air *Plasma Sources Sci. Technol.* **28** 09LT02

[48] Chng T L, Orel I S, Starikovskaia S M and Adamovich I V 2019 Electric field induced second harmonic (E-FISH)

generation for characterization of fast ionization wave discharges at moderate and low pressures *Plasma Sources Sci. Technol.* **28** 045004
[49] Orr K, Tang Y, Simeni M S, van den Bekerom D and Adamovich I V 2020 Measurements of electric field in an atmospheric pressure helium plasma jet by the E-FISH method *Plasma Sources Sci. Technol.* **29** 035019
[50] Adamovich I V, Butterworth T, Orriere T, Pai D Z, Lacoste D A and Cha M S 2020 Nanosecond second harmonic generation for electric field measurements with temporal resolution shorter than laser pulse duration *J. Phys. D: Appl. Phys.* **53** 145201
[51] Huang B, Zhang C, Adamovich I, Akishev Y and Shao T 2020 Surface ionization wave propagation in the nanosecond pulsed surface dielectric barrier discharge: the influence of dielectric material and pulse repetition rate *Plasma Sources Sci. Technol.* **29** 044001
[52] Lepikhin N D, Luggenhölscher D and Czarnetzki U 2020 Electric field measurements in a He: N_2 nanosecond pulsed discharge with sub-ns time resolution *J. Phys. D: Appl. Phys.* **54** 055201
[53] Müller S, Luggenhölscher D and Czarnetzki U 2011 Ignition of a nanosecond-pulsed near atmospheric pressure discharge in a narrow gap *J. Phys. D: Appl. Phys.* **44** 165202
[54] Böhm P, Kettlitz M, Brandenburg R, Höft H and Czarnetzki U 2016 Determination of the electric field strength of filamentary DBDs by CARS-based four-wave mixing *Plasma Sources Sci. Technol.* **25** 054002
[55] Roy S, Meyer T R, Lucht R P, Afzelius M, Bengtsson P E and Gord J R 2004 Dual-pump dual-broadband coherent anti-stokes Raman scattering in reacting flows *Opt. Lett.* **29** 1843–5
[56] Tedder S A, Wheeler J L and Danehy P M 2011 Characteristics of a broadband dye laser using pyrromethene and rhodamine dyes *Appl. Opt.* **50** 901–14
[57] Eckbreth A C 1996 *Laser Diagnostics for Combustion Temperature and Species* (*Combustion Science and Technology Book Series*) vol 3, 2nd edn (Boca Raton: CRC Press)
[58] Hagelaar G J M and Pitchford L C 2005 Solving the Boltzmann equation to obtain electron transport coefficients and rate coefficients for fluid models *Plasma Sources Sci. Technol.* **14** 722–33
[59] Alves L L 2014 The IST-LISBON database on LXCat *J. Phys.: Conf. Ser.* **565** 012007
[60] Donkó Z, Schulze J, Müller S and Czarnetzki U 2011 Kinetic simulation of a nanosecond-pulsed hydrogen microdischarge *Appl. Phys. Lett.* **98** 251502
[61] Lo C and Hamaguchi S 2011 Dynamics of near-atmospheric-pressure hydrogen plasmas driven by pulsed high voltages *IEEE Trans. Plasma Sci.* **39** 2100–1
[62] Lo C W and Hamaguchi S 2011 Numerical analyses of hydrogen plasma generation by nanosecond pulsed high voltages at near-atmospheric pressure *J. Phys. D: Appl. Phys.* **44** 375201
[63] Fedotov A B, Naumov A N, Silin V P, Uryupin S A, Zheltikov A M, Tarasevitch A P and von der Linde D 2000 Third-harmonic generation in a laser-pre-excited gas: the role of excited-state neutrals *Phys. Lett.* A **271** 407–12